Supporting Information

A coverage-corrected energetic span descriptor for comparing CO_2 hydrogenation activity and selectivity on Cu–In surfaces

Yu Zhang[a], Xinxin Tian[*,b,c] and Shuanglin Qu[*,a]

[a] College of Chemistry and Chemical Engineering, Hunan University, Changsha 410082, P. R. China
[b] Institute of Molecular Science, Key Laboratory of Chemical Biology and Molecular Engineering of Ministry of Education, Shanxi University, Taiyuan 030006, P. R. China
[c] Shanxi Key Laboratory for the Green Catalysis Synthesis of Coal-based Value-added Chemicals, School of Chemistry and Chemical Engineering, Shanxi University, Taiyuan 030006, P. R. China

Corresponding Author:
Xinxin Tian: tianxx@sxu.edu.cn; Shuanglin Qu: squ@hnu.edu.cn

Table of Contents

1. Computational model

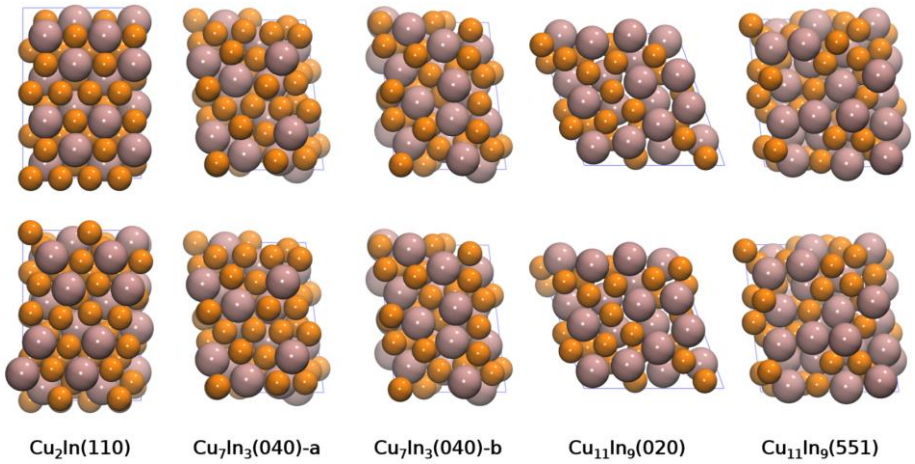

Fig. S1. Surfaces of the five Cu−In alloys: (top row) freshly cleaved surfaces and (bottom row) the corresponding surfaces after structural relaxation. Orange and coral spheres denote Cu and In atoms, respectively.

2. Microkinetic analysis and adsorption energetics

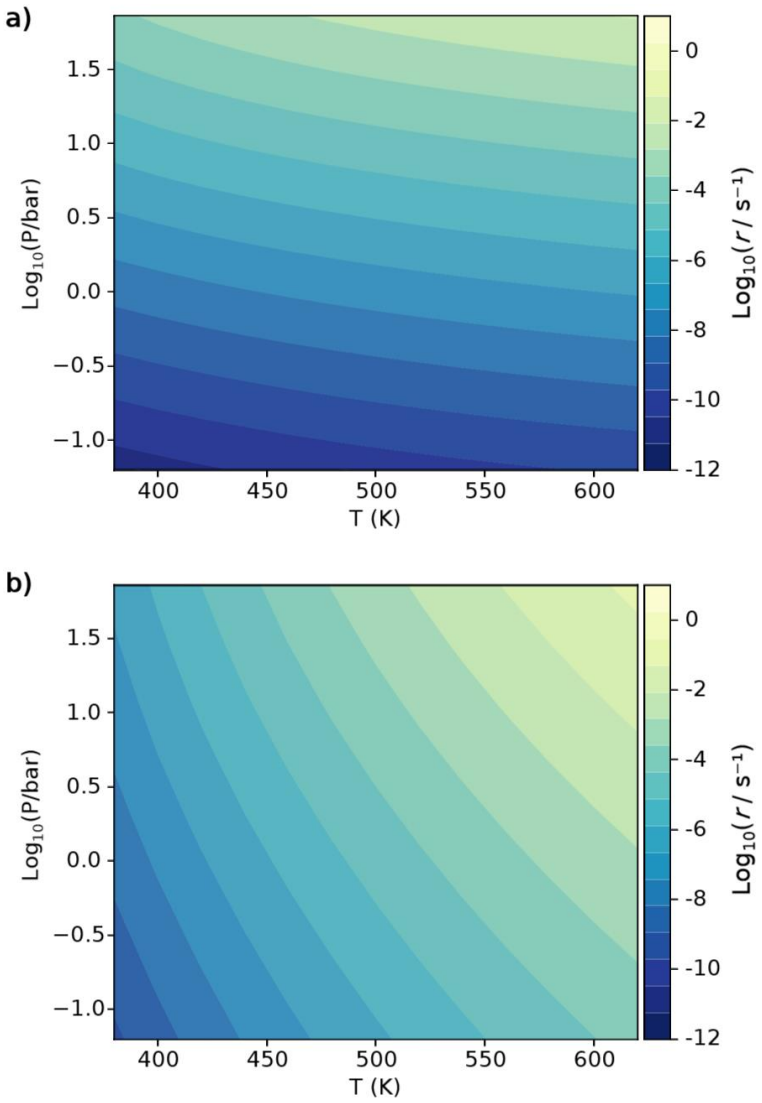

Fig. S2. Two-dimensional reaction rate maps for the formation of (a) methanol and (b) CO on the $Cu_2In(110)$ surface as a function of temperature and pressure. Reaction rates are presented on a logarithmic (log_{10}) scale, as indicated by the color bar on the right.

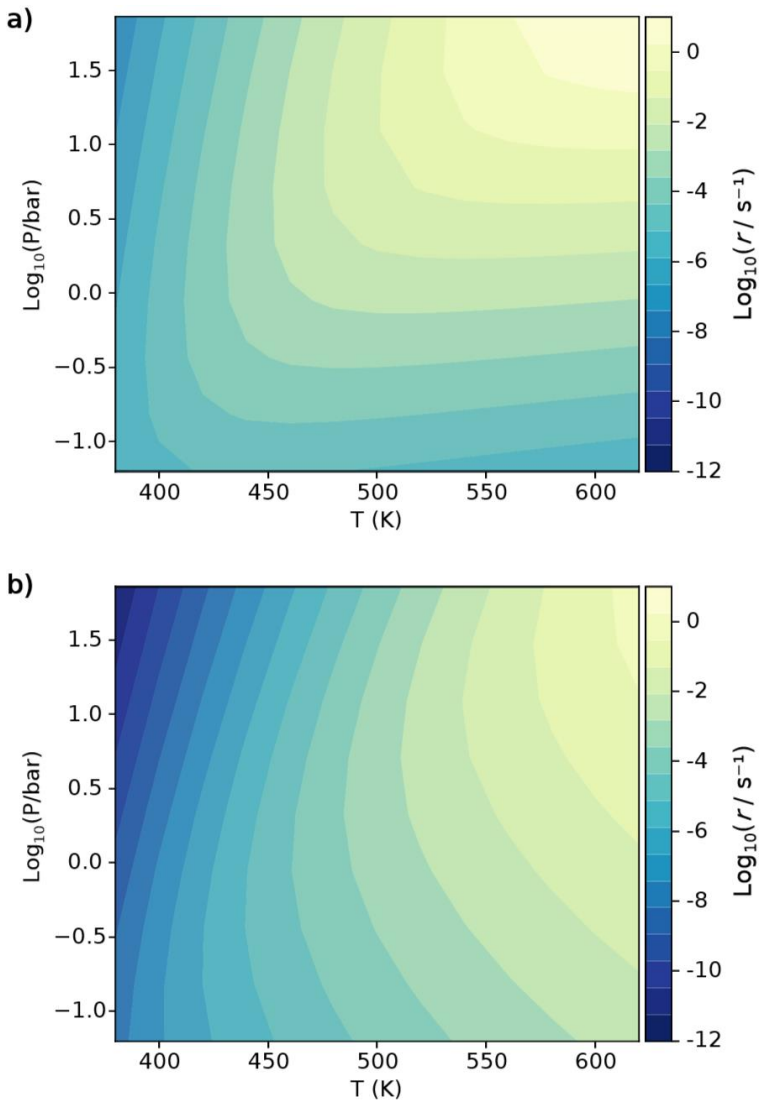

Fig. S3. Two-dimensional reaction rate maps for the formation of (a) methanol and (b) CO on the $Cu_7In_3(040)$-a surface as a function of temperature and pressure. Reaction rates are presented on a logarithmic (log_{10}) scale, as indicated by the color bar on the right.

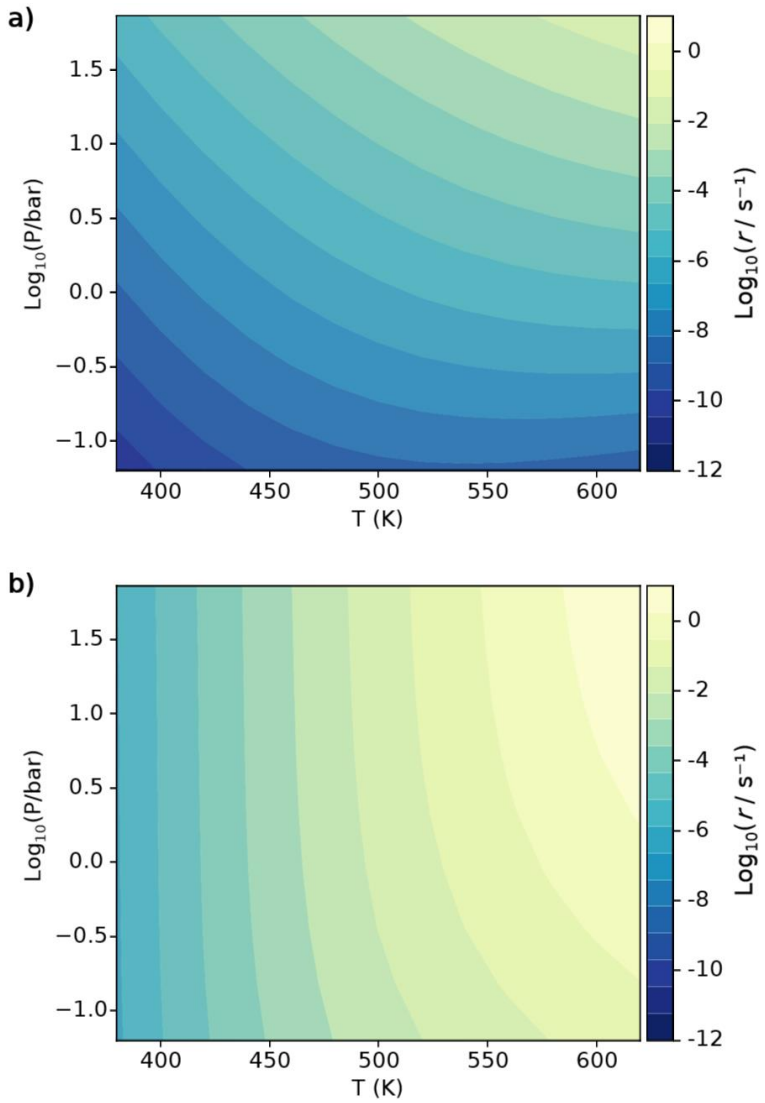

Fig. S4. Two-dimensional reaction rate maps for the formation of (a) methanol and (b) CO on the Cu_7In_3(040)-b surface as a function of temperature and pressure. Reaction rates are presented on a logarithmic (log_{10}) scale, as indicated by the color bar on the right.

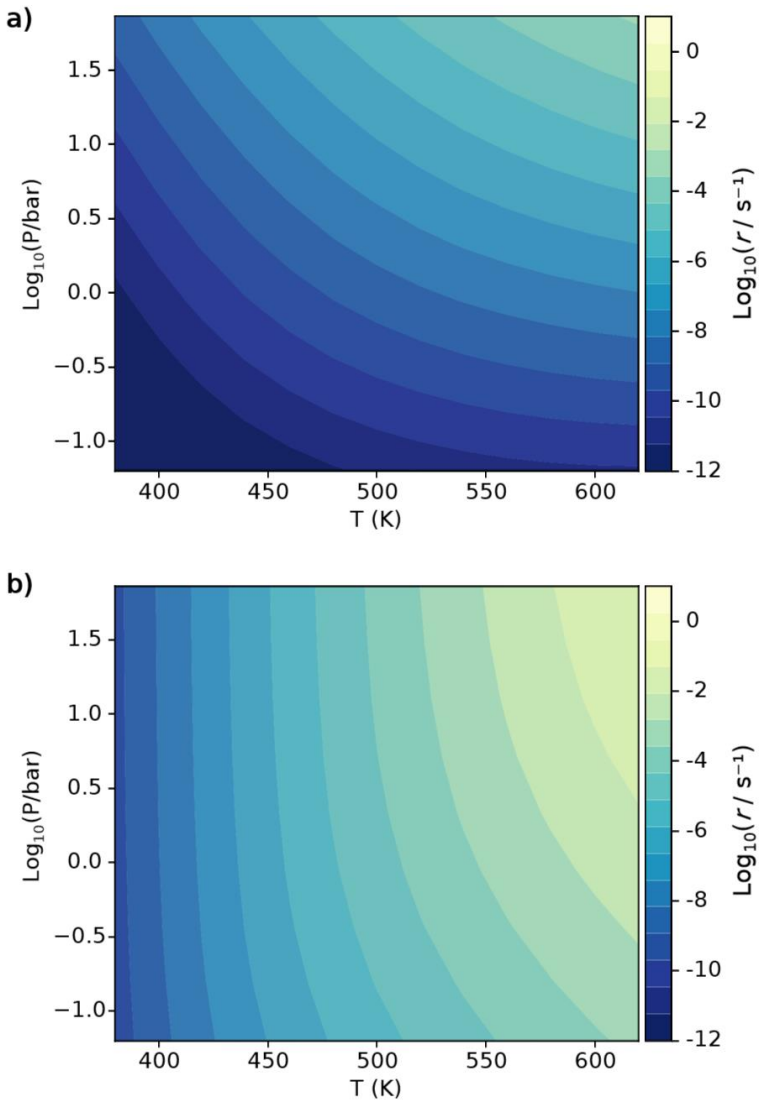

Fig. S5. Two-dimensional reaction rate maps for the formation of (a) methanol and (b) CO on the $Cu_{11}In_9(020)$ surface as a function of temperature and pressure. Reaction rates are presented on a logarithmic (log_{10}) scale, as indicated by the color bar on the right.

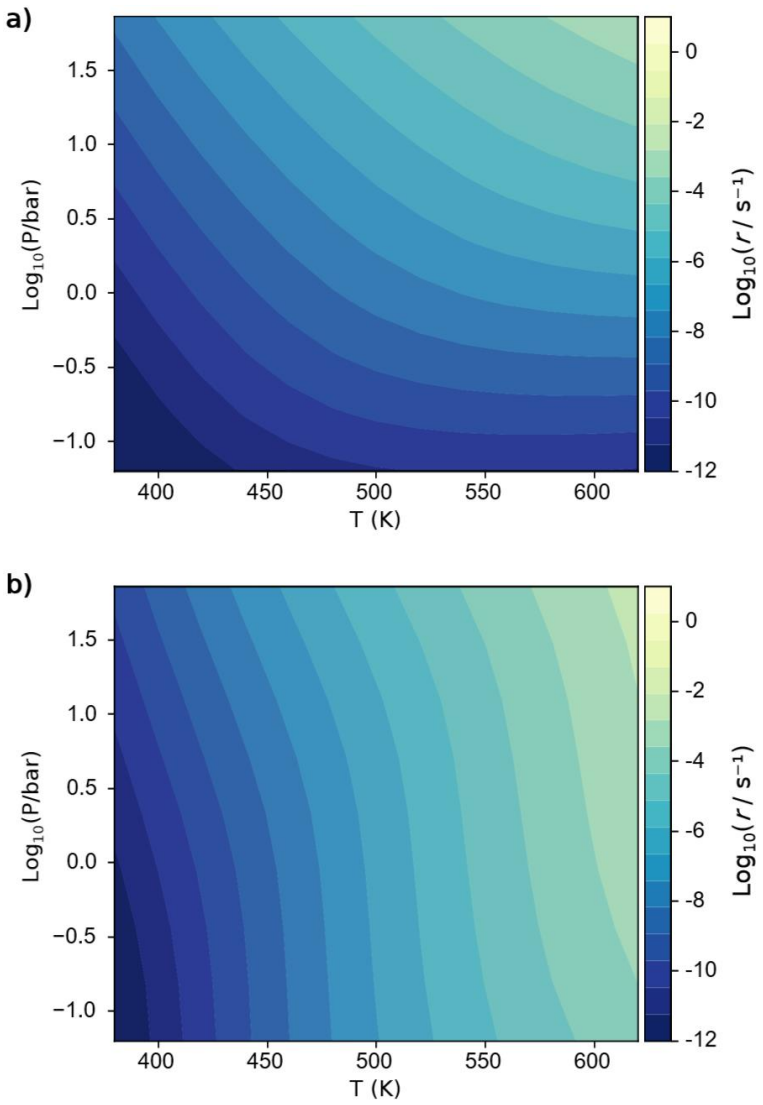

Fig. S6. Two-dimensional reaction rate maps for the formation of (a) methanol and (b) CO on the $Cu_{11}In_9(551)$ surface as a function of temperature and pressure. Reaction rates are presented on a logarithmic (log_{10}) scale, as indicated by the color bar on the right.

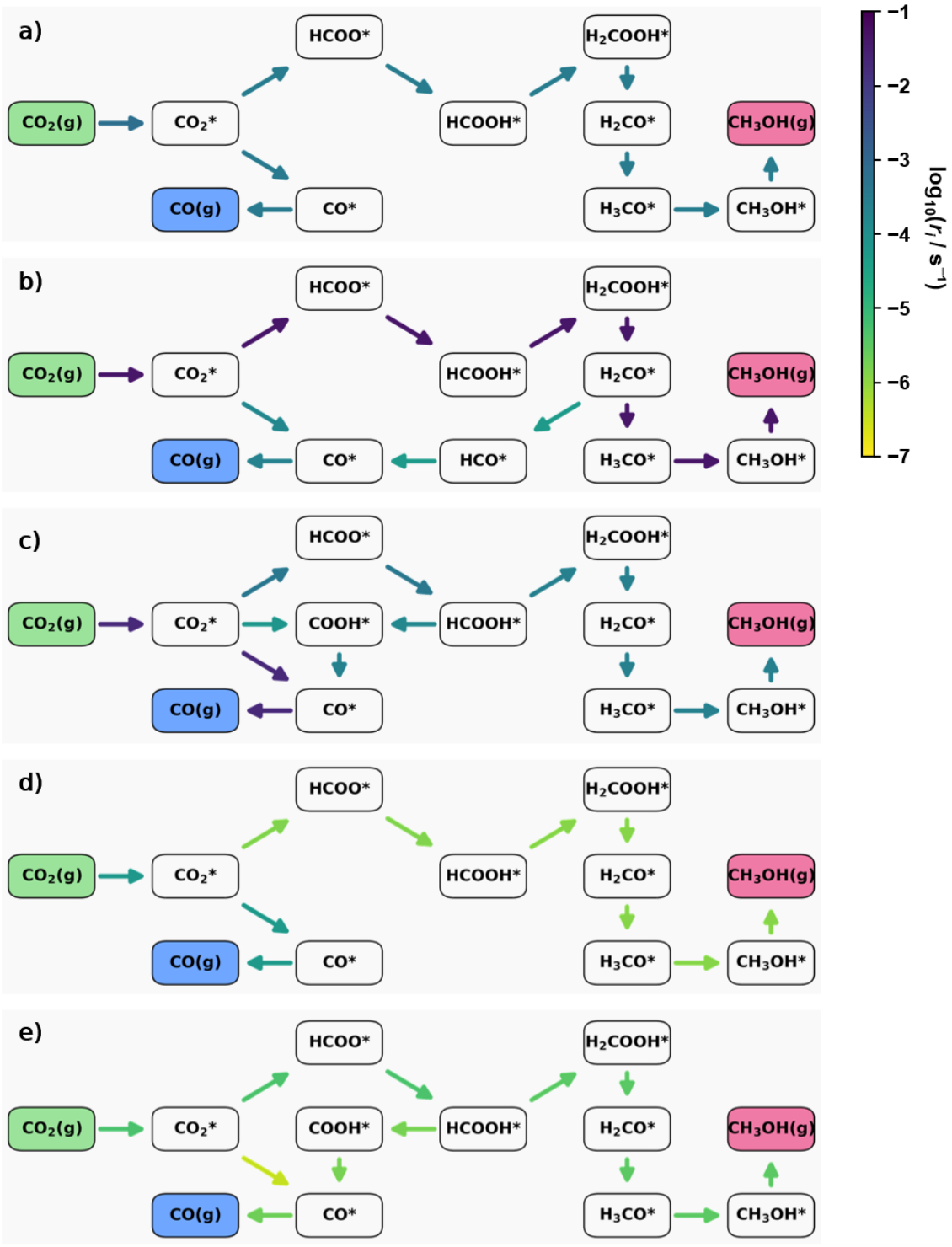

Fig. S7. Dominant reaction pathway diagrams on (a) $Cu_2In(110)$, (b) $Cu_7In_3(040)$-a, (c) $Cu_7In_3(040)$-b, (d) $Cu_{11}In_9(020)$, and (e) $Cu_{11}In_9(551)$ at 500 K under partial pressures of 22.5 bar H_2 and 7.5 bar CO_2. Arrow shading reflects the reaction rate of each elementary step, with darker arrows indicating faster rates. For clarity, steps with the lowest absolute or relative rates on each surface have been omitted.

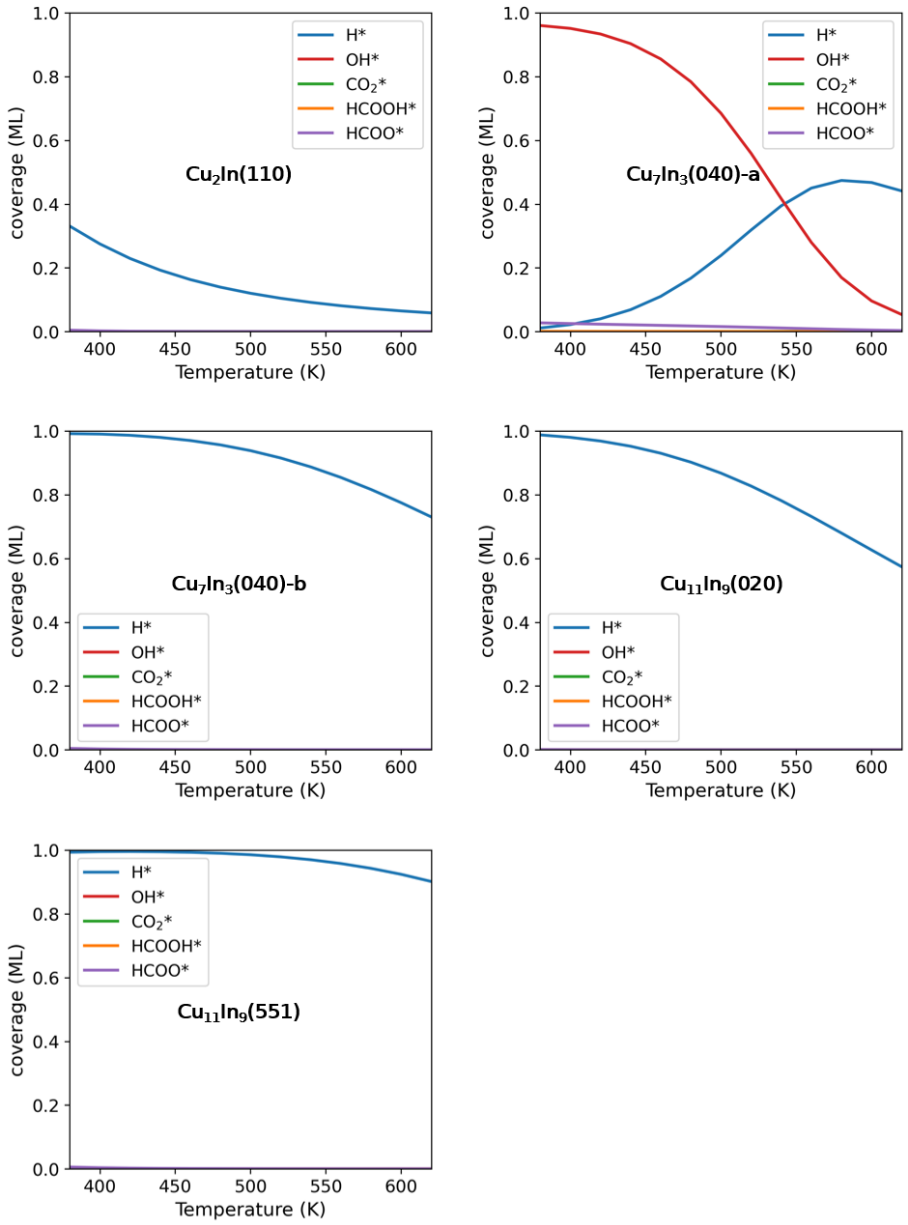

Fig. S8. Calculated steady-state coverages of the major adsorbed species (H*, OH*, CO_2*, HCOOH*, and HCOO*) on the $Cu_2In(110)$, $Cu_7In_3(040)$-a, $Cu_7In_3(040)$-b, $Cu_{11}In_9(020)$, and $Cu_{11}In_9(551)$ under reaction conditions with H_2 and CO_2 partial pressures of 22.5 and 7.5 bar, respectively.

Table S1. The net reaction rate (r_i) of elementary reaction steps from microkinetic modeling for CO_2 activation on various Cu−In alloy surfaces at 500 K and 30 bar. Columns (a−e) correspond to $Cu_2In(110)$, $Cu_7In_3(040)$-a, $Cu_7In_3(040)$-b, $Cu_{11}In_9(020)$, and $Cu_{11}In_9(551)$, respectively.

	step *i*	a	b	c	d	e
R1	$CO_2(g) + * \rightarrow CO_2*$	6.77E-04	4.49E-02	2.06E-02	6.16E-05	5.41E-06
R2	$H_2(g) + 2* \rightarrow 2H*$	9.74E-04	1.34E-01	1.03E-02	2.19E-05	1.19E-05
R3	$CO_2* + H* \rightarrow HCOO* + *$	3.27E-04	4.48E-02	4.24E-04	1.39E-06	5.07E-06
R4	$HCOO* + H* \rightarrow H_2COO* + *$	2.67E-07	1.96E-13	5.37E-10	7.17E-10	5.03E-10
R5	$HCOO* + H* \rightarrow HCOOH* + *$	3.26E-04	4.48E-02	4.24E-04	1.38E-06	5.07E-06
R6	$H_2COO* + H* \rightarrow H_2COOH* + *$	2.67E-07	1.96E-13	5.37E-10	7.17E-10	5.03E-10
R7	$HCOOH* + H* \rightarrow H_2COOH* + *$	3.23E-04	4.48E-02	2.56E-04	1.26E-06	3.37E-06
R8	$HCOOH* + * \rightarrow HCO* + OH*$	9.94E-10	1.73E-08	1.02E-10	1.87E-11	6.05E-11
R9	$H_2COOH* + * \rightarrow H_2CO* + OH*$	3.24E-04	4.48E-02	2.56E-04	1.26E-06	3.37E-06
R10	$HCO* + H* \rightarrow H_2CO* + *$	−2.65E-08	−5.80E-05	−1.57E-07	−4.53E-09	−4.56E-08
R11	$H_2CO* + H* \rightarrow H_3CO* + *$	3.24E-04	4.47E-02	2.56E-04	1.25E-06	3.32E-06
R12	$OH* + H* \rightarrow H_2O* + *$	6.77E-04	4.49E-02	2.06E-02	6.16E-05	5.41E-06
R13	$H_3CO* + H* \rightarrow CH_3OH* + *$	3.24E-04	4.47E-02	2.56E-04	1.25E-06	3.32E-06
R14	$CO_2* + H* \rightarrow COOH* + *$	3.72E-09	7.08E-07	7.55E-05	2.90E-07	1.54E-08
R15	$CO_2* + * \rightarrow CO* + O*$	3.50E-04	1.69E-04	2.01E-02	5.99E-05	3.30E-07
R16	$COOH* + * \rightarrow CO* + OH*$	2.94E-06	4.86E-06	2.44E-04	4.18E-07	1.72E-06
R17	$CO* + H* \rightarrow HCO* + *$	−2.75E-08	−5.80E-05	−1.57E-07	−4.55E-09	−4.57E-08
R18	$CO* \rightarrow CO(g) + *$	3.53E-04	2.31E-04	2.03E-02	6.03E-05	2.09E-06
R19	$O* + H* \rightarrow OH* + *$	5.16E-08	−6.77E-10	9.29E-03	1.77E-05	1.51E-07
R20	$CH_3OH* \rightarrow CH_3OH(g) + *$	3.24E-04	4.47E-02	2.56E-04	1.25E-06	3.32E-06
R21	$H_2O* \rightarrow H_2O(g) + *$	6.77E-04	4.49E-02	2.06E-02	6.16E-05	5.41E-06
R22	$COOH* + H* \rightarrow HCOOH* + *$	−2.94E-06	−4.15E-06	−1.68E-04	−1.28E-07	−1.70E-06
R23	$H_2(g) + O* + * \rightarrow OH*+ H*$	3.50E-04	1.69E-04	1.08E-02	4.22E-05	1.79E-07

Note: The net rates of the H_2COO*-involving steps, including **R4** ($HCOO* + H* \rightarrow H_2COO* + *$) and **R6** ($H_2COO* + H* \rightarrow H_2COOH* +*$), are several orders of magnitude lower than those of the dominant $HCOO* + H* \rightarrow HCOOH* +*$ (**R5**) hydrogenation route on all investigated surfaces. Therefore, the H_2COO* pathway was excluded from the dominant reaction mechanism.

Table S2. Preferred adsorption sites and the corresponding Gibbs free energies and enthalpies of adsorption [in brackets] for CO_2, H, CO, H_2O, and MeOH at 500 K under reaction conditions of 7.5 bar CO_2, 22.5 bar H_2, and 1 bar each of CO, H_2O, and MeOH. For clarity, only top-layer atoms are shown on all surfaces. The orange, brown, red, gray, and white spheres represent Cu atom, In atom, O atom, C atom, and H atom, respectively.

	CO_2	H	CO	H_2O	MeOH
$Cu_2In(110)$	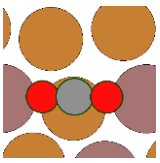 +0.51 [−0.23]	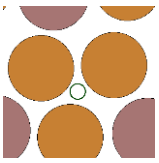 +0.09 [−0.16]	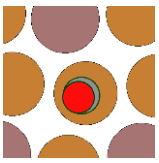 +0.21 [−0.53]	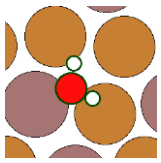 +0.39 [−0.25]	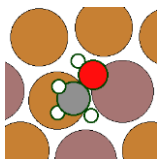 +0.28 [−0.36]
$Cu_7In_3(040)$-a	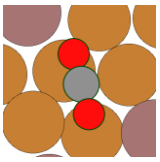 +0.22 [−0.35]	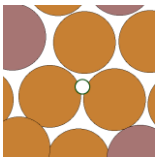 −0.06 [−0.34]	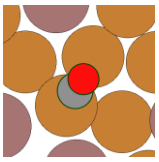 −0.17 [−0.75]	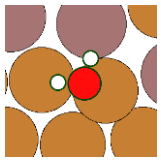 −0.07 [−0.59]	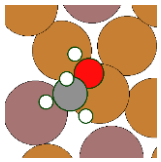 +0.03 [−0.72]
$Cu_7In_3(040)$-b	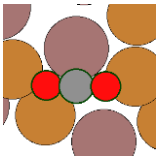 +0.35 [−0.23]	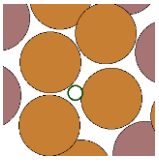 −0.12 [−0.38]	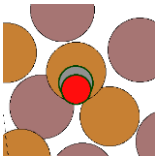 −0.23 [−0.80]	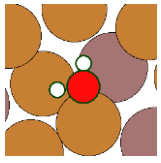 −0.04 [−0.67]	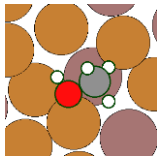 −0.13 [−0.85]
$Cu_{11}In_9(020)$	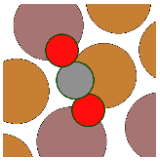 +0.35 [−0.29]	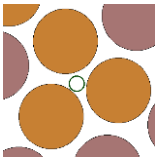 −0.08 [−0.35]	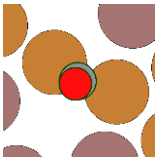 −0.14 [−0.71]	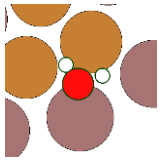 +0.38 [−0.23]	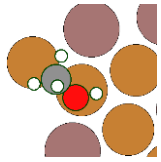 +0.25 [−0.44]
$Cu_{11}In_9(551)$	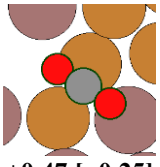 +0.47 [−0.25]	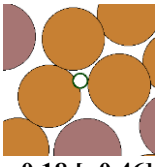 −0.18 [−0.46]	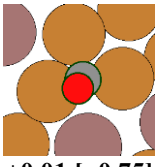 +0.01 [−0.75]	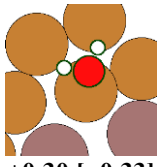 +0.30 [−0.33]	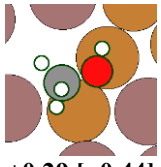 +0.29 [−0.44]

Note:

At 500 K, CO_2 adsorption is thermodynamically unfavorable on all investigated Cu−In surfaces, whereas H* adsorption is comparatively strong on all surfaces except $Cu_2In(110)$. Adsorption of MeOH and H_2O is also generally unfavorable, indicating facile product desorption under reaction conditions. The anomalous behavior observed on $Cu_2In(110)$ can be attributed to pronounced surface reconstruction effects (Fig. S1). Specifically, the In−In distance decreases from 3.67 to 3.21 Å. Along the

−In−Cu−In−Cu− chain oriented along the *a* direction of the surface unit cell, the Cu−In bond lengths are elongated from 2.65 to 2.80 Å; the two Cu_4 linear chains become distorted and no longer maintain a coplanar 180° configuration, while the In−Cu−In angle between adjacent Cu_4 chains decreases from 90° to 70°.

Table S3. Degree of kinetic rate control ($X_{RC,i}$) for some important elementary reaction steps ($|X_{RC,i}| > 0.1$) involved in the formation of MeOH, CO, and H_2O from CO_2 activation on the $Cu_2In(110)$.

adsorbed species	$X_{RC,i}$		
	MeOH	CO	H_2O
H*	−0.25	−0.24	−0.24
CO−O*	0.00	0.99	0.52
H−HCOOH*	0.99	0.00	0.48

Table S4. Degree of kinetic rate control ($X_{RC,i}$) for some important elementary reaction steps ($|X_{RC,i}| > 0.1$) involved in the formation of MeOH, CO, and H_2O from CO_2 activation on the $Cu_7In_3(040)$-a.

adsorbed species	$X_{RC,i}$		
	MeOH	CO	H_2O
H*	−0.46	−0.46	−0.46
OH*	−1.35	−1.36	−1.35
CO−O*	0.00	0.73	0.00
H−H_2CO*	−0.15	−0.72	−0.15
H−HCOOH*	0.00	−0.16	−0.09
H−HCO*	0.00	0.25	0.00
H−OH*	1.23	0.91	1.23

Table S5. Degree of kinetic rate control ($X_{RC,i}$) for some important elementary reaction steps ($|X_{RC,i}| > 0.1$) involved in the formation of MeOH, CO, and H_2O from CO_2 activation on the $Cu_7In_3(040)$-b.

adsorbed species	$X_{RC,i}$		
	MeOH	CO	H_2O
H*	−1.91	−1.88	−1.88
CO−O*	0.00	0.99	0.98
H−HCOOH*	0.99	0.00	0.00

Table S6. Degree of kinetic rate control ($X_{RC,i}$) for some important elementary reaction steps ($|X_{RC,i}| > 0.1$) involved in the formation of MeOH, CO, and H_2O from CO_2 activation on the $Cu_{11}In_9(020)$.

adsorbed species	$X_{RC,i}$		
	MeOH	CO	H_2O
H*	−1.76	−1.73	−1.73
CO−O*	0.00	0.99	0.97
H−HCOOH*	0.99	0.00	0.00

Table S7. Degree of kinetic rate control ($X_{RC,i}$) for some important elementary reaction steps ($|X_{RC,i}| > 0.1$) involved in the formation of MeOH, CO, and H_2O from CO_2 activation on the $Cu_{11}In_9(551)$.

adsorbed species	$X_{RC,i}$		
	MeOH	CO	H_2O
H*	−1.97	−1.97	−1.97
CO−O*	0.00	0.16	0.00
H−COOH*	0.00	0.81	0.31
H−HCOOH*	0.79	0.00	0.49
H_2CO−OH*	0.21	0.00	0.13

Note: The X_{RC} values for H_2O formation are reported for completeness because H_2O is a co-product of both methanol synthesis and CO formation pathways. These values help identify the role of OH* and H_2O* species in the overall reaction network, although the main discussion focuses on the formation of the target products, CH_3OH and CO.

3. Free-energy profiles and representative structures

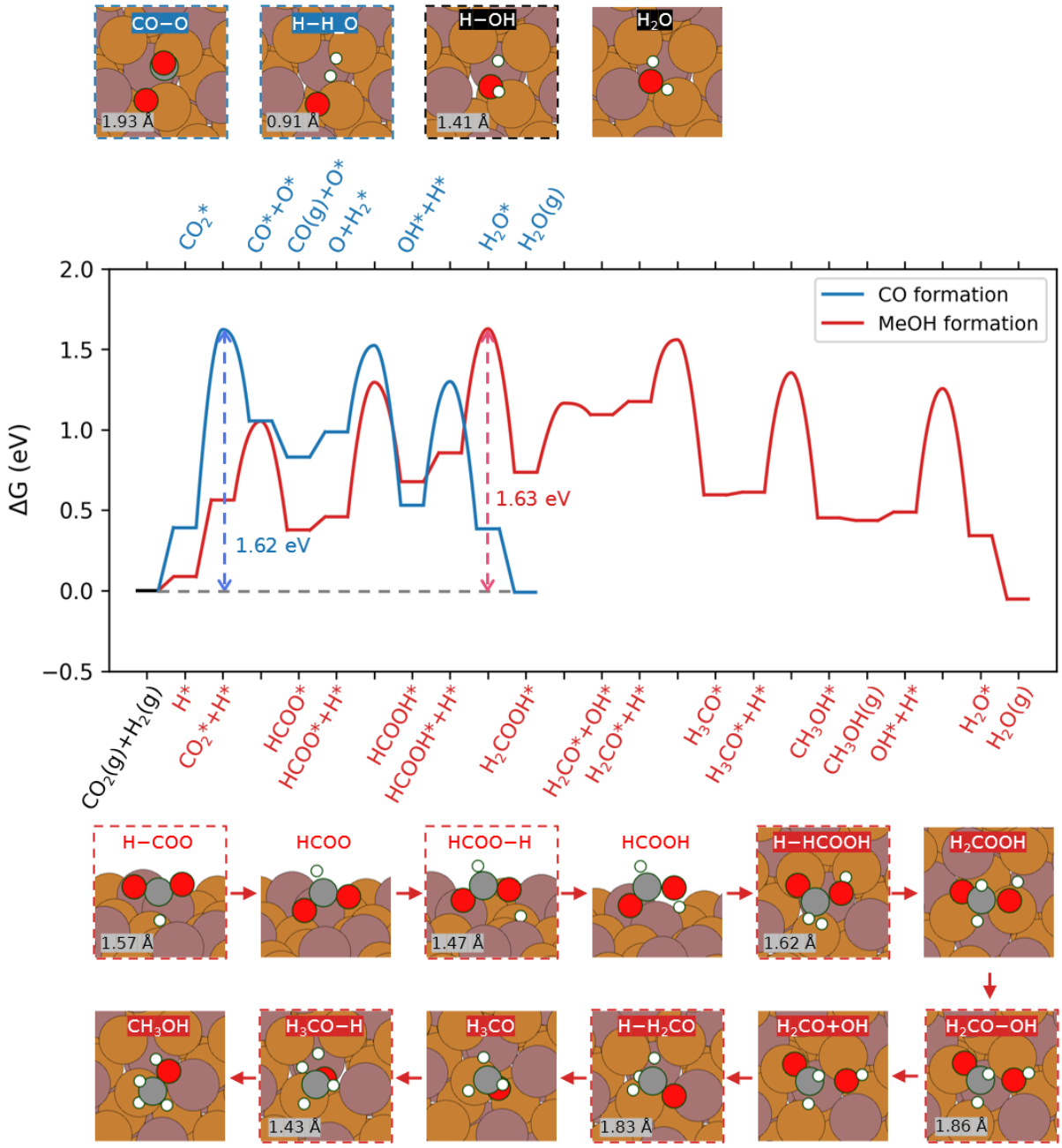

Fig. S9. Gibbs free energy diagram and optimized structures of reaction intermediates and transition states for methanol and CO formation on $Cu_2In(110)$ at 500 K under reaction conditions of 22.5 bar H_2, 7.5 bar CO_2, and 1 bar each of CO, H_2O, and MeOH. Orange, brown, red, gray, and white spheres denote Cu, In, O, C, and H atoms, respectively; transition-state structures are outlined by dashed boxes.

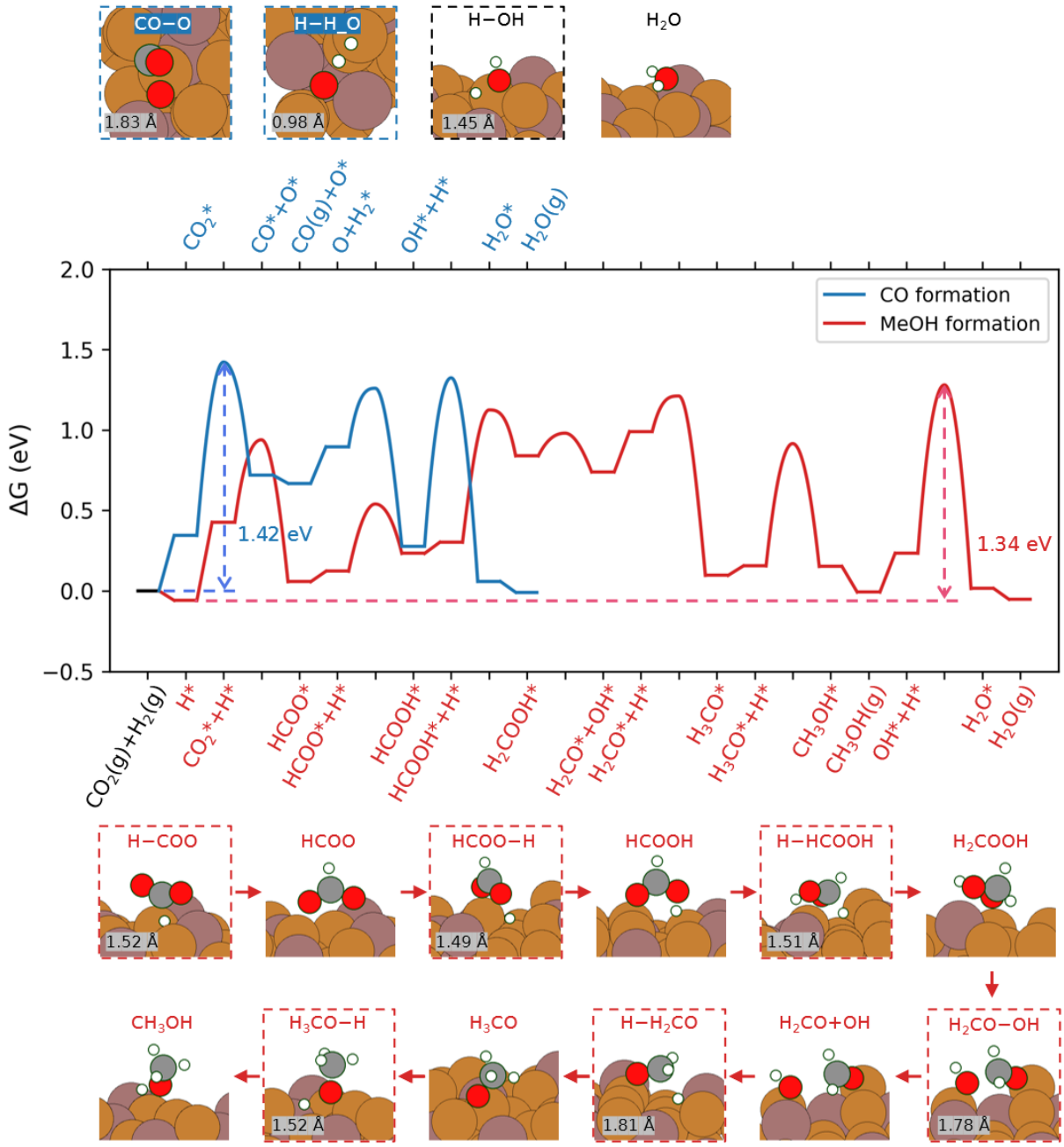

Fig. S10. Gibbs free energy diagram and optimized structures of reaction intermediates and transition states for methanol and CO formation on Cu_7In_3(040)-a at 500 K under reaction conditions of 22.5 bar H_2, 7.5 bar CO_2, and 1 bar each of CO, H_2O, and MeOH. Orange, brown, red, gray, and white spheres denote Cu, In, O, C, and H atoms, respectively; transition-state structures are outlined by dashed boxes.

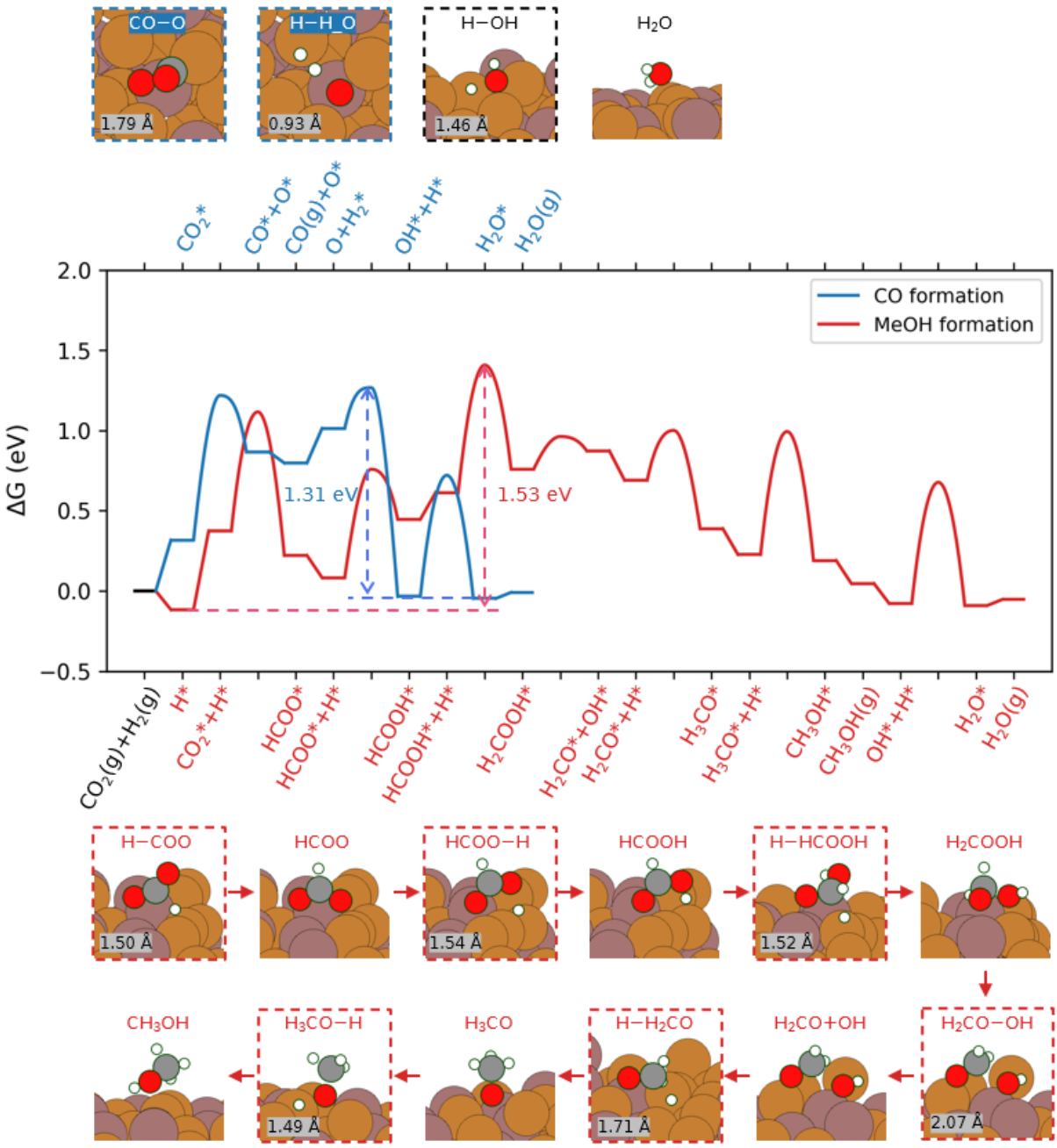

Fig. S11. Gibbs free energy diagram and optimized structures of reaction intermediates and transition states for methanol and CO formation on $Cu_7In_3(040)$-b at 500 K under reaction conditions of 22.5 bar H_2, 7.5 bar CO_2, and 1 bar each of CO, H_2O, and MeOH. Orange, brown, red, gray, and white spheres denote Cu, In, O, C, and H atoms, respectively; transition-state structures are outlined by dashed boxes.

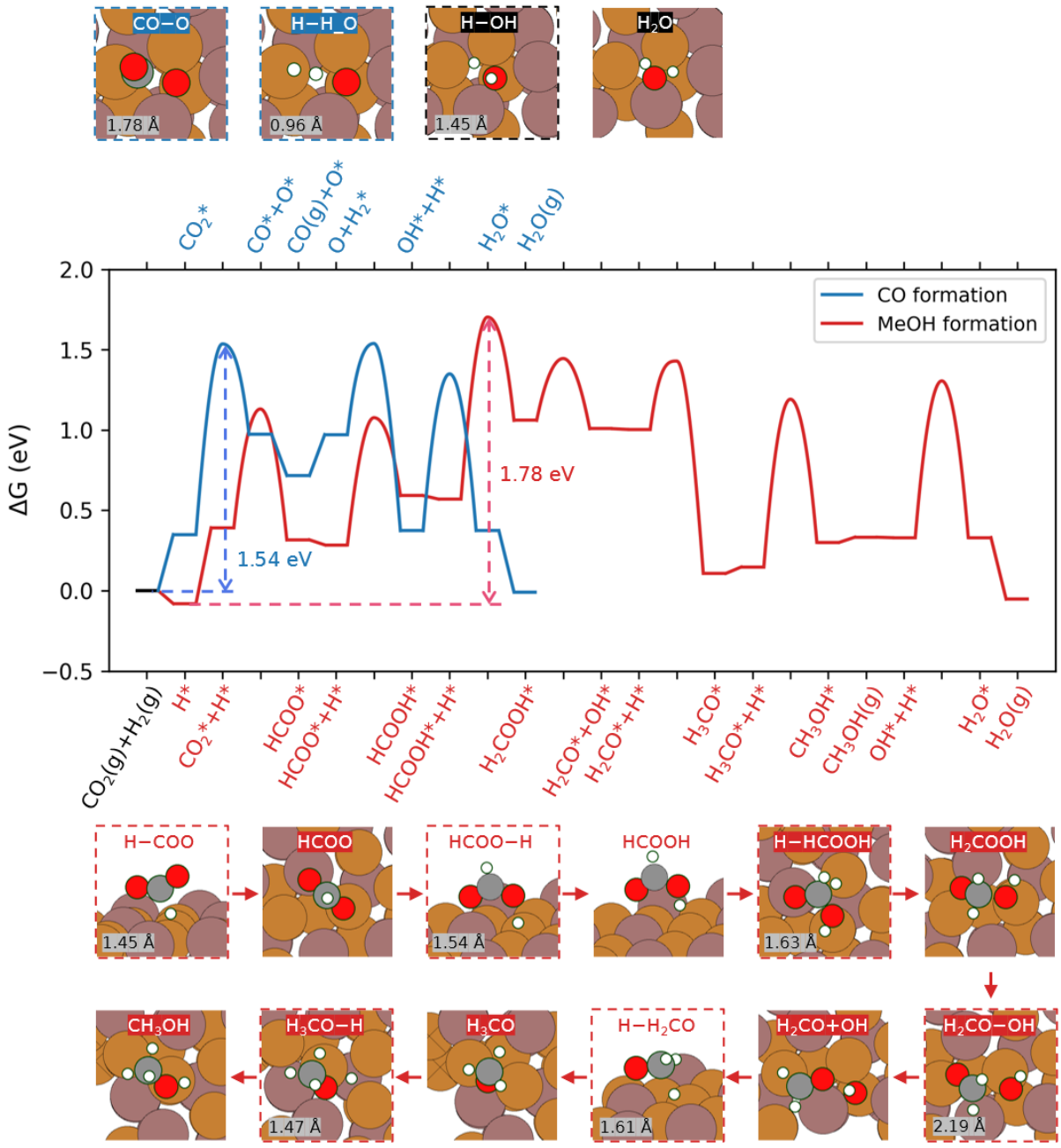

Fig. S12. Gibbs free energy diagram and optimized structures of reaction intermediates and transition states for methanol and CO formation on $Cu_{11}In_9(020)$ at 500 K under reaction conditions of 22.5 bar H_2, 7.5 bar CO_2, and 1 bar each of CO, H_2O, and MeOH. Orange, brown, red, gray, and white spheres denote Cu, In, O, C, and H atoms, respectively; transition-state structures are outlined by dashed boxes.

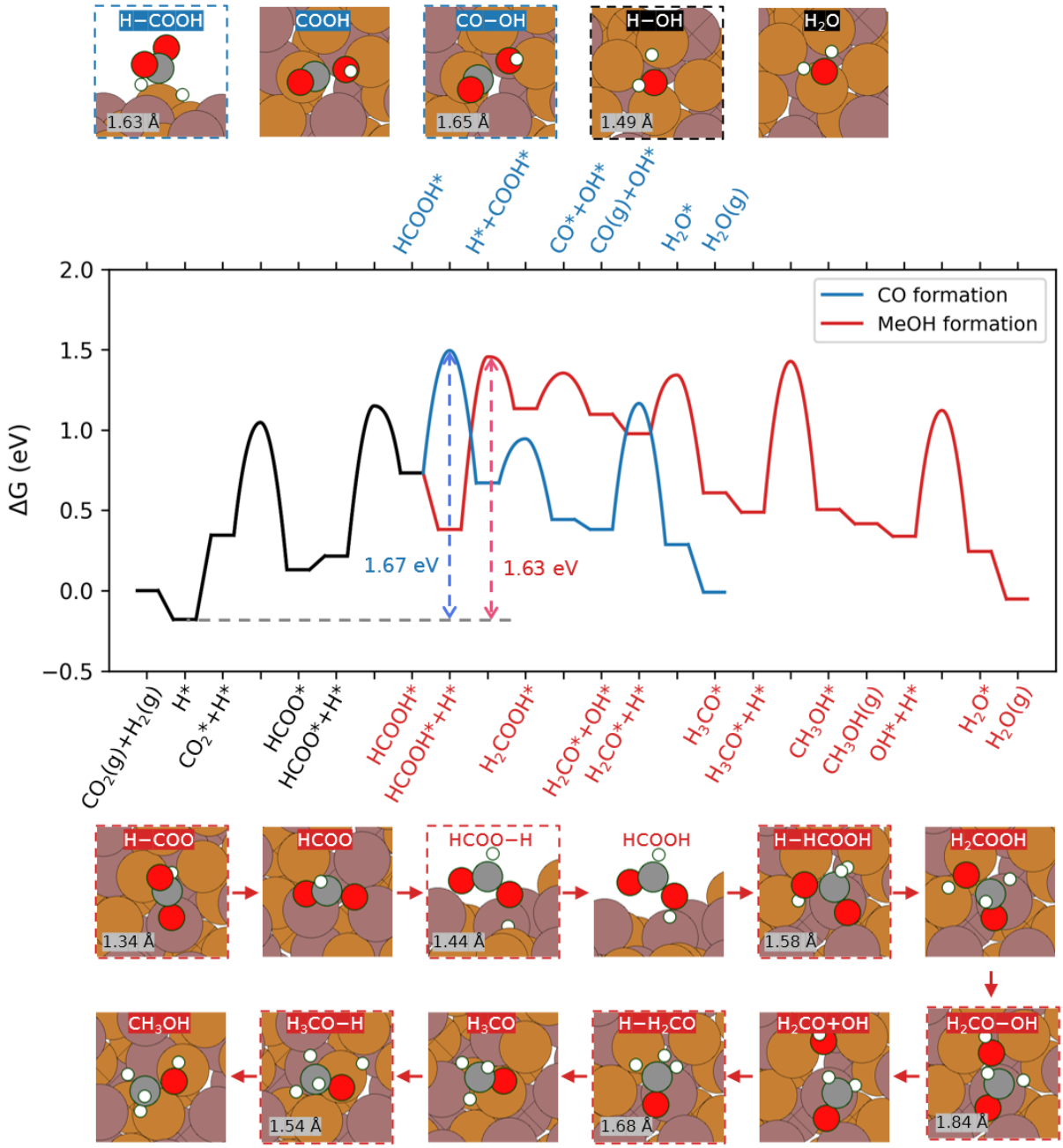

Fig. S13. Gibbs free energy diagram and optimized structures of reaction intermediates and transition states for methanol and CO formation on $Cu_{11}In_9(551)$ at 500 K under reaction conditions of 22.5 bar H_2, 7.5 bar CO_2, and 1 bar each of CO, H_2O, and MeOH. Orange, brown, red, gray, and white spheres denote Cu, In, O, C, and H atoms, respectively; transition-state structures are outlined by dashed boxes.

4. Activity descriptors and free energies of formation

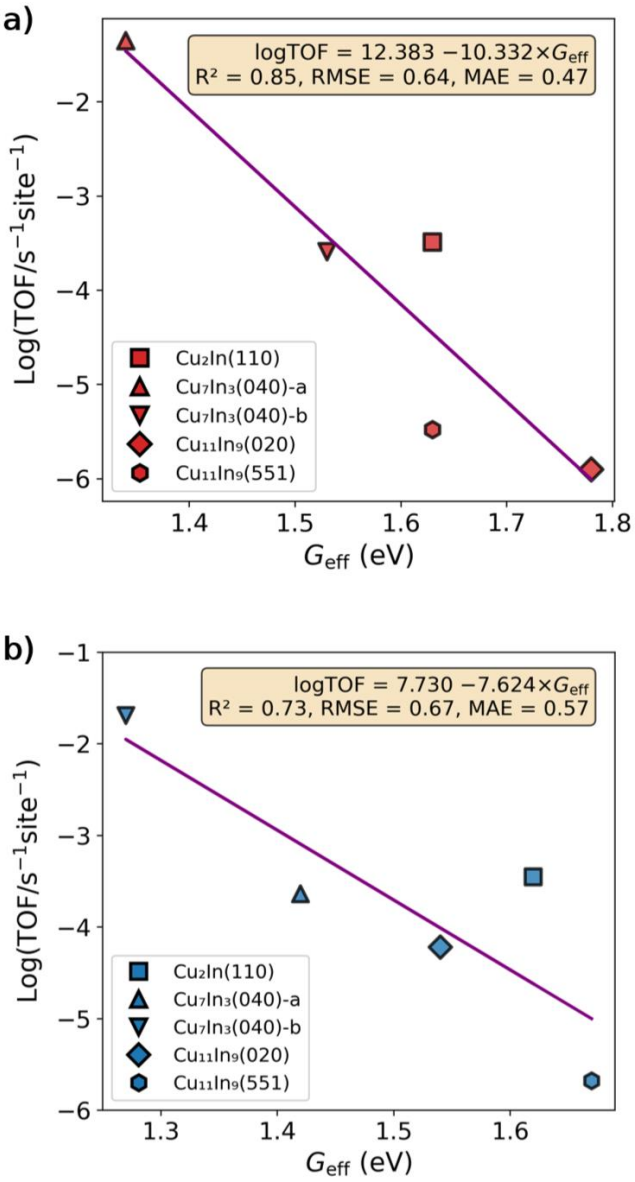

Fig. S14. Correlation between the logarithm of the reaction rates and the conventional PES-based effective barrier (G_{eff}) for methanol (a) and CO (b) formation across five Cu−In surfaces at 500 K.

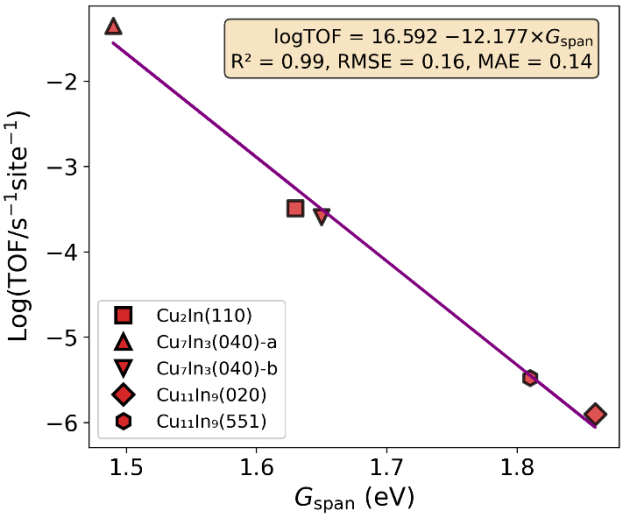

Fig. S15. Correlation between the logarithm of the reaction rates and the TDI-corrected energetic span (G_{span}) for methanol formation across five Cu−In surfaces at 500 K.

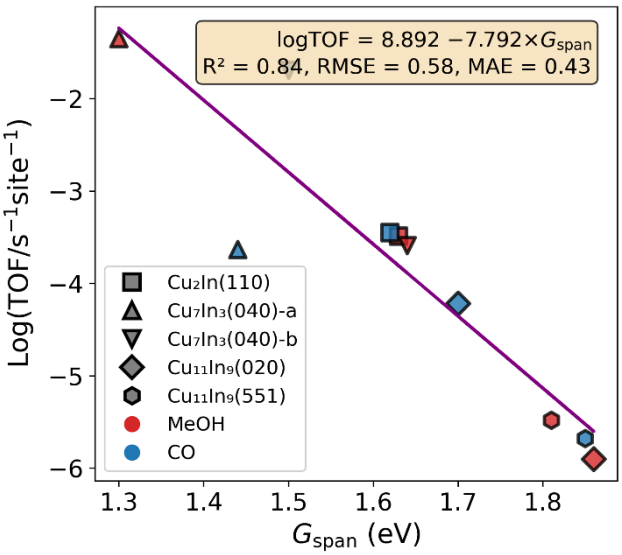

Fig. S16. Correlation between the logarithm of the reaction rates and G_{span} values recalculated using MKM-derived dominant surface species as the thermodynamic baseline across five Cu−In surfaces at 500 K.

Note: For Cu_7In_3(040)-a at 500 K, OH* was used as the baseline according to the steady-state coverage and DRC analysis, while the dominant surface species identified from MKM were used for the remaining surfaces. The resulting correlation (R^2 = 0.84) is weaker than that obtained using the PES-based G_{span} values, indicating that the dominant steady-state surface species from MKM cannot be directly substituted for the PES-derived thermodynamic baseline in this simplified energetic span descriptor.

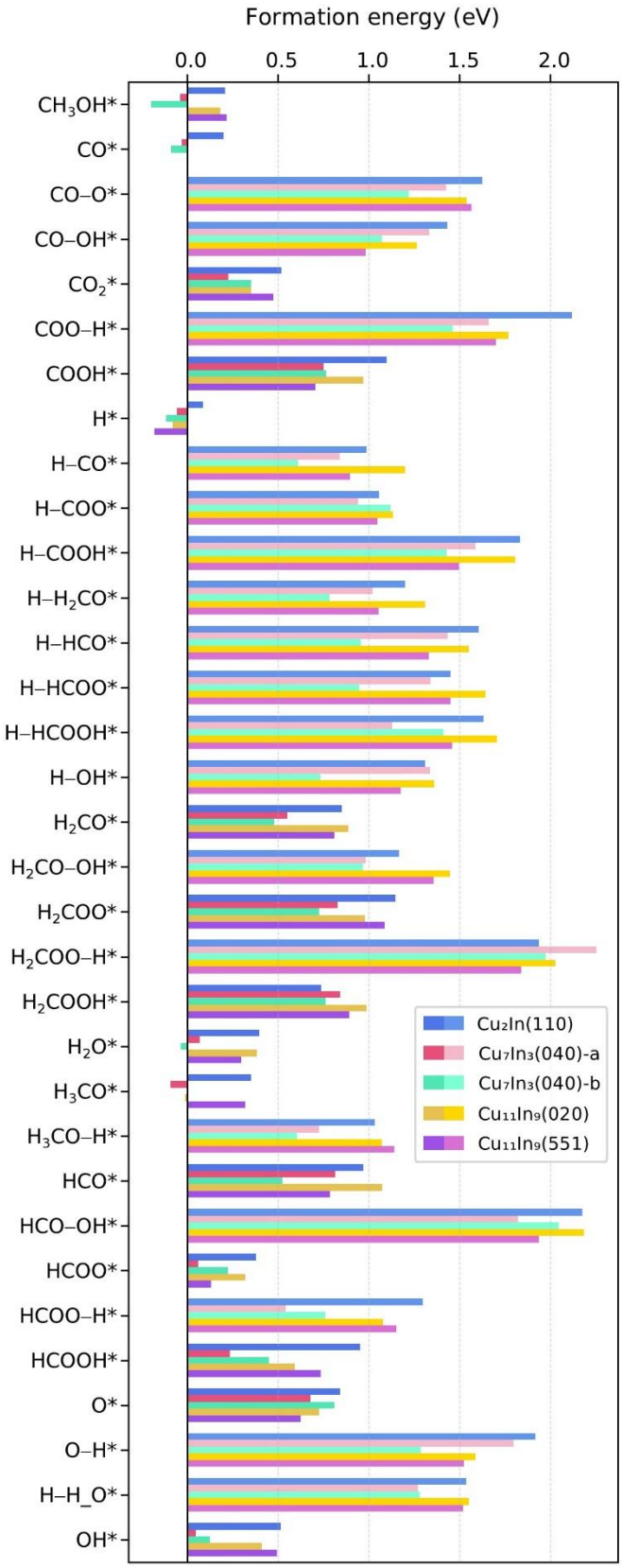

Fig. S17. Relative Gibbs free energies of formation of surface intermediates and transition states at 500 K, evaluated with respect to the gas-phase chemical potentials (H_2, CO_2, H_2O) under reaction conditions with partial pressures of 22.5 bar H_2, 7.5 bar CO_2, and 1 bar each of CO, H_2O, and MeOH. Dark-colored bars denote intermediates, while light-colored bars represent transition states.

Note:

For a general surface species $C_aH_bO_c$*, where *a*, *b*, and *c* are the numbers of C, H, and O atoms, respectively, the Gibbs free energy of formation is given by:

$$\Delta G_{\mathrm{form}}(\mathrm{C}_a\mathrm{H}_b\mathrm{O}_c^*) = G(\mathrm{C}_a\mathrm{H}_b\mathrm{O}_c^*) - G(\mathrm{slab}) - aR_C - bR_H - cR_O$$

The elemental reference energies are defined as:

$$R_H = \frac{1}{2}\mu_{\mathrm{H_2}}$$

$$R_O = \mu_{\mathrm{H_2O}} - \mu_{\mathrm{H_2}}$$

$$R_C = \mu_{\mathrm{CO_2}} - 2R_O = \mu_{\mathrm{CO_2}} - 2\mu_{\mathrm{H_2O}} + 2\mu_{\mathrm{H_2}}$$

where $\mu_{\mathrm{H_2}}$, $\mu_{\mathrm{H_2O}}$, and $\mu_{\mathrm{CO_2}}$ correspond to the chemical potentials of gas-phase H_2, H_2O, and CO_2, respectively, under the specified reaction conditions.

Expanding the elemental reference energies gives:

$$\Delta G_{\mathrm{form}}(\mathrm{C}_a\mathrm{H}_b\mathrm{O}_c^*) = G(\mathrm{C}_a\mathrm{H}_b\mathrm{O}_c^*) - G(\mathrm{slab}) - a\mu_{\mathrm{CO_2}} + (2a - c)\mu_{\mathrm{H_2O}} - \left(2a + \frac{b}{2} - c\right)\mu_{\mathrm{H_2}}$$

This expression shows that the explicit contribution from $\mu_{\mathrm{H_2O}}$ depends on the stoichiometric coefficient ($2a - c$), rather than affecting all oxygen-containing species equally.

For example, for HCOO*, where $a = 1$, $b = 1$, and $c = 2$, the Gibbs free energy of formation is:

$$\Delta G_{\mathrm{form}}(\mathrm{HCOO}^*) = G(\mathrm{HCOO}^*) - G(\mathrm{slab}) - R_C - R_H - 2R_O$$

which can be expanded as:

$$\Delta G_{\mathrm{form}}(\mathrm{HCOO}^*) = G(\mathrm{HCOO}^*) - G(\mathrm{slab}) - \mu_{\mathrm{CO_2}} - \frac{1}{2}\mu_{\mathrm{H_2}}$$

Therefore, the $\mu_{\mathrm{H_2O}}$ term is cancelled for HCOO*. The same cancellation applies to other COO-containing intermediates, such as H_2COO*, HCOOH*, and H_2COOH*. In contrast, more reduced oxygen-containing species, such as CO*, HCO*, H_2CO*, H_3CO*, CH_3OH*, OH*, and H_2O*, retain an explicit dependence on the selected oxygen reference and are therefore more sensitive to the thermodynamic contribution of H_2O.

For instance, the formation free energy of H_3CO* can be expanded as:

$$\Delta G_{\mathrm{form}}(\mathrm{H_3CO}^*) = G(\mathrm{H_3CO}^*) - G(\mathrm{slab}) - \mu_{\mathrm{CO_2}} + \mu_{\mathrm{H_2O}} - \frac{5}{2}\mu_{\mathrm{H_2}}$$

This explains why highly reduced oxygen-containing intermediates, such as H_3CO*, can be more sensitive to the chosen oxygen reference than COO-containing species. The same procedure was applied to all other surface intermediates and transition states.

Alternative reference schemes were also examined as consistency checks. An O_2-based oxygen reference led to a strong systematic stabilization of nearly all surface intermediates and transition states, which is not representative of the H_2-rich CO_2 hydrogenation environment considered here. A CH_4/H_2-based carbon reference was also tested, but it introduces a highly reduced carbon reservoir outside the

present CO_2/H_2 reaction network and changes the TDTS assignment for Cu_7In_3(040)-a. Moreover, O_2 and CH_4 are not involved as reactant or product reservoirs in the present CO_2/H_2 hydrogenation network, whereas the adopted H_2O/H_2-based reference uses species directly participating in the reaction system. Therefore, the H_2O/H_2-based oxygen reference was adopted because it is more consistent with the CO_2/H_2-based PES and descriptor framework used in this work.

Table S8. Summary of TDI/baseline assignments in MKM and descriptor analyses for methanol and CO formation at 500 K.

Surface	MKM-inferred TDI	G_{span} baseline	G_{HL} TDI
$Cu_2In(110)$	H*	Reference state	Reference state
$Cu_7In_3(040)$-a	OH*	H*	H*
$Cu_7In_3(040)$-b	H*	H*	H*
$Cu_{11}In_9(020)$	H*	H*	H*
$Cu_{11}In_9(551)$	H*	H*	H*

Note: The MKM-inferred TDI was assigned based on steady-state coverages and DRC analysis. The G_{span} baseline denotes the thermodynamic reference adopted in the corrected energetic span analysis for both methanol and CO formation. "Reference state" refers to the clean surface plus gas-phase reactants, corresponding to $G_{TDI} = 0$ on the adopted free-energy scale.

Table S9. Summary of TDTS assignments in MKM and descriptor analyses for methanol and CO formation at 500 K.

Surface	MKM TDTS		G_{span} TDTS		G_{HL} TDTS	
	MeOH	CO	MeOH	CO	MeOH	CO
$Cu_2In(110)$	H−HCOOH*	CO−O*	H−HCOOH*	CO−O*	H−HCOOH*	CO−O*
$Cu_7In_3(040)$-a	H−OH*	H−OH*	H−OH*	CO−O*	H−OH*	CO−O*
$Cu_7In_3(040)$-b	H−HCOOH*	CO−O*	H−HCOOH*	H−H_O*	H−HCOOH*	H−H_O*
$Cu_{11}In_9(020)$	H−HCOOH*	CO−O*	H−HCOOH*	CO−O*	H−HCOOH*	CO−O*
$Cu_{11}In_9(551)$	H−HCOOH*	H−COOH*	H−HCOOH*	H−COOH*	H−HCOOH*	H−COOH*

Note: TDTS denotes the transition state controlling the corresponding reaction channel. For CO formation on $Cu_7In_3(040)$-b, H−H_O* and CO−O* differ by only 0.06 eV and are therefore considered nearly degenerate.

Table S10. Summary of energetic descriptors for methanol and CO formation on five Cu−In surfaces at 500 K.

Surface	G_{eff}		G_{span}		G_{HL}	
	MeOH	CO	MeOH	CO	MeOH	CO
$Cu_2In(110)$	1.63	1.62	1.63	1.62	1.63	1.62
$Cu_7In_3(040)$-a	1.34	1.42	1.40	1.54	1.45	1.54
$Cu_7In_3(040)$-b	1.53	1.31	1.64	1.50	1.64	1.51
$Cu_{11}In_9(020)$	1.78	1.54	1.86	1.70	1.86	1.70
$Cu_{11}In_9(551)$	1.63	1.67	1.81	1.85	1.82	1.86

Note: G_{eff} is the conventional PES-derived energetic span; G_{span} is the TDI-corrected energetic span including the site-requirement correction; and G_{HL} is the descriptor obtained from the Gibbs formation-energy scheme using the identified TDTS and TDI. All values are given in eV under the descriptor-analysis conditions.

5. Identification of the preferred reaction pathway

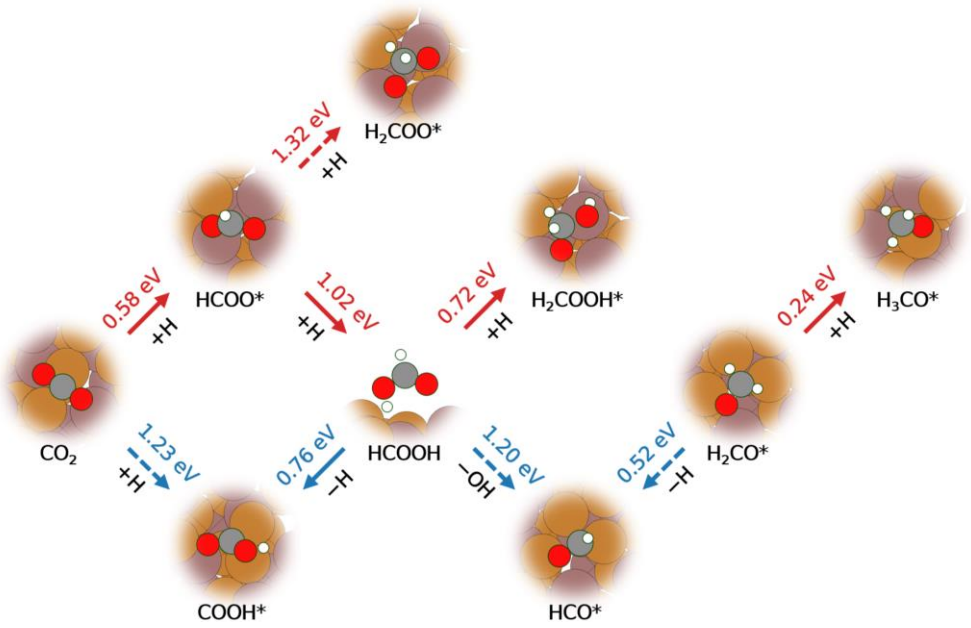

Fig. S18. Branching pathways at the $Cu_{11}In_9$(551) for methanol and CO formation. Red and blue arrows denote the methanol and CO formation pathways, respectively; dashed arrows indicate kinetically unfavorable pathways, and the numbers on the arrows represent the energy barriers according to the branched reaction energy diagram for each step. The color scheme of atoms: Cu, orange; In, brown; O, red; C, gray; H, white.

Note:

Starting from CO_2, hydrogenation preferentially proceeds via the H−COO* transition state to form HCOO*, which is kinetically favored over the alternative COOH-forming pathway. Subsequent hydrogenation of HCOO* preferentially yields HCOOH* rather than H_2COO*, consistent with the lower free energy of the corresponding transition state. From HCOOH*, continued hydrogenation toward H_2COOH* is kinetically favored over dehydrogenation or direct C−O bond cleavage, ultimately leading to methanol formation. The alternative CO formation pathway proceeds via dehydrogenation to COOH* followed by C−O bond cleavage, in agreement with the TDTS assignments discussed in the main text.

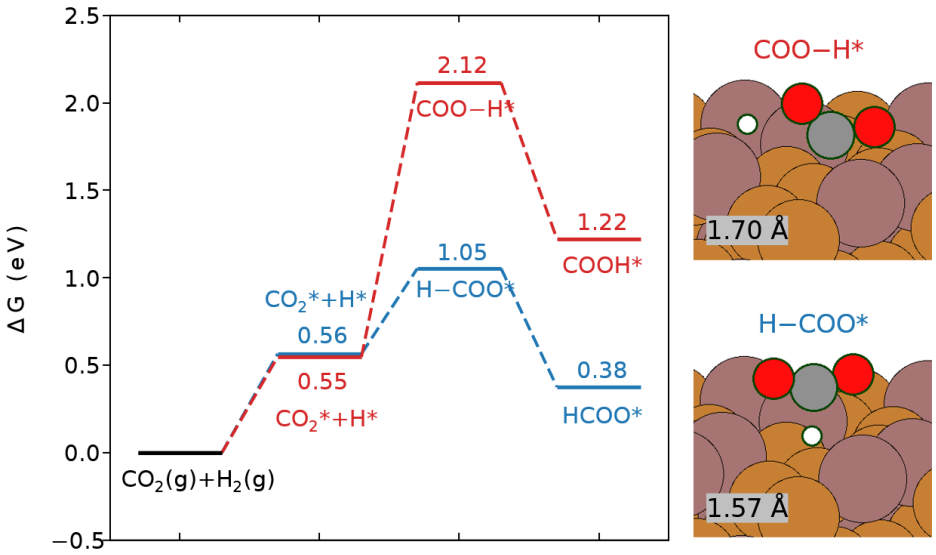

Fig. S19. Gibbs free energy diagram and transition state structures for the initial steps of CO_2 hydrogenation on $Cu_2In(110)$ at 500 K under partial pressures of 22.5 bar H_2 and 7.5 bar CO_2. The color scheme of atoms is as follows: Cu, orange; In, brown; O, red; C, gray; H, white.

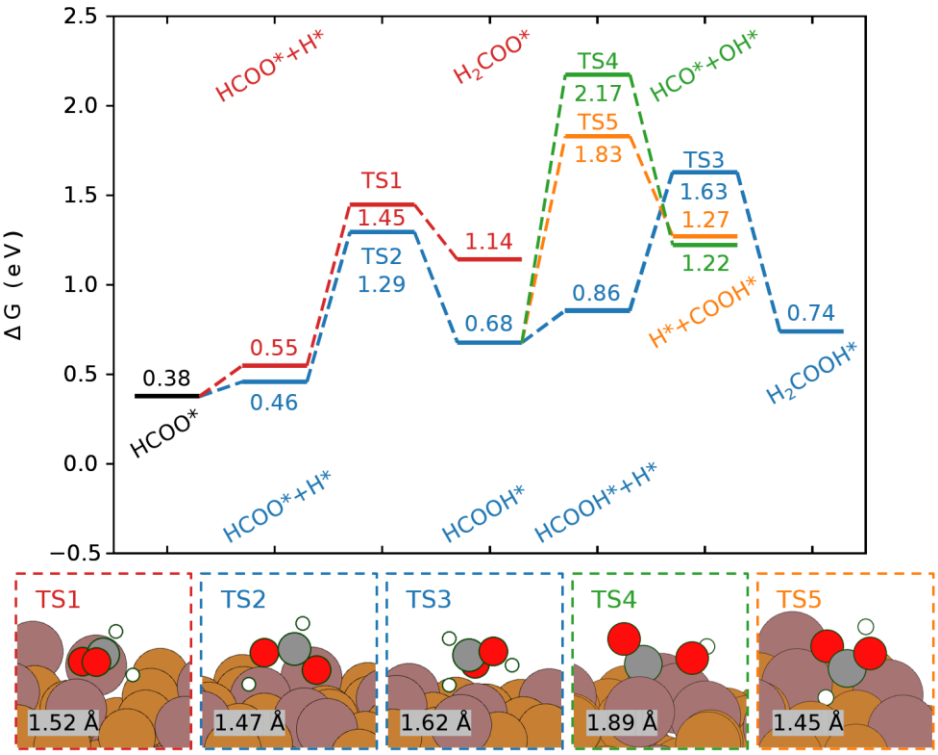

Fig. S20. Gibbs free energy diagram and representative transition state structures for competing reaction pathways originating from HCOO* on $Cu_2In(110)$ at 500 K, including hydrogenation and dissociation routes relevant to CO_2 hydrogenation. The color scheme of atoms: Cu, orange; In, brown; O, red; C, gray; H, white.

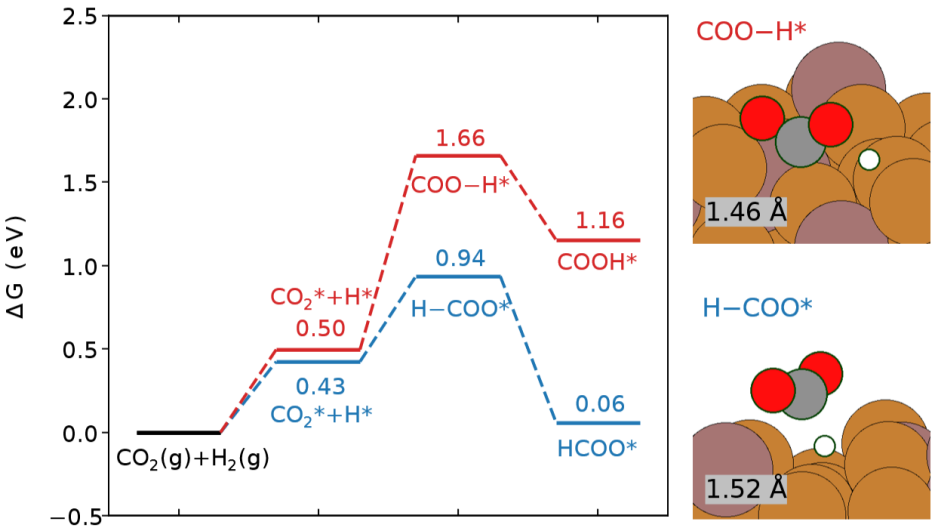

Fig. S21. Gibbs free energy diagram and transition state structures for the initial steps of CO_2 hydrogenation on Cu_7In_3(040)-a at 500 K under partial pressures of 22.5 bar H_2 and 7.5 bar CO_2. The color scheme of atoms is as follows: Cu, orange; In, brown; O, red; C, gray; H, white.

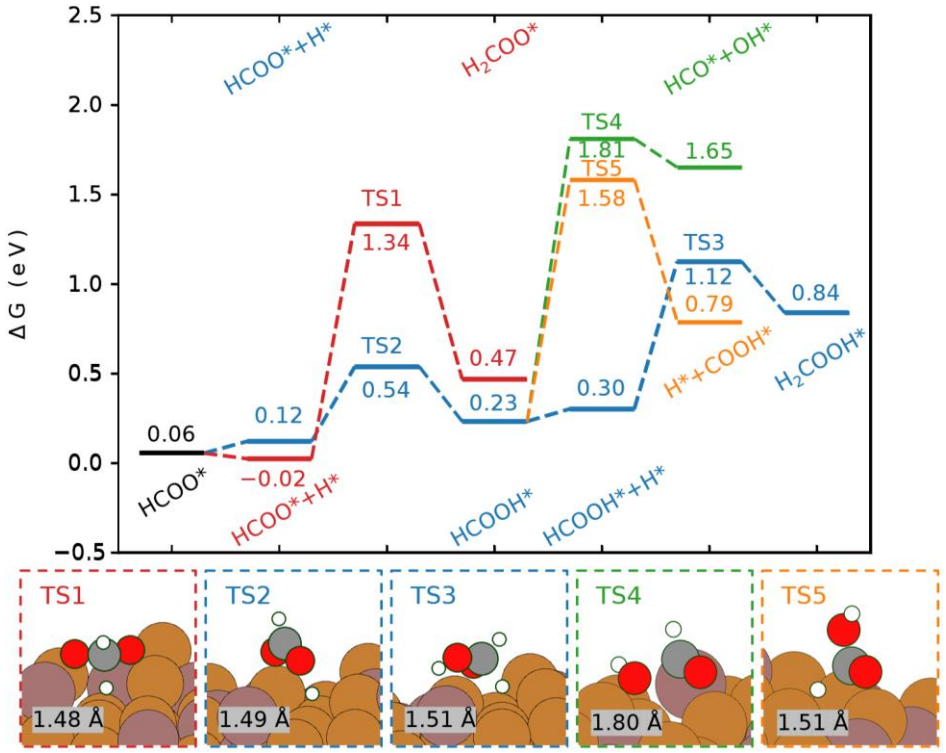

Fig. S22. Gibbs free energy diagram and representative transition state structures for competing reaction pathways originating from HCOO* on Cu_7In_3(040)-a at 500 K, including hydrogenation and dissociation routes relevant to CO_2 hydrogenation. The color scheme of atoms: Cu, orange; In, brown; O, red; C, gray; H, white.

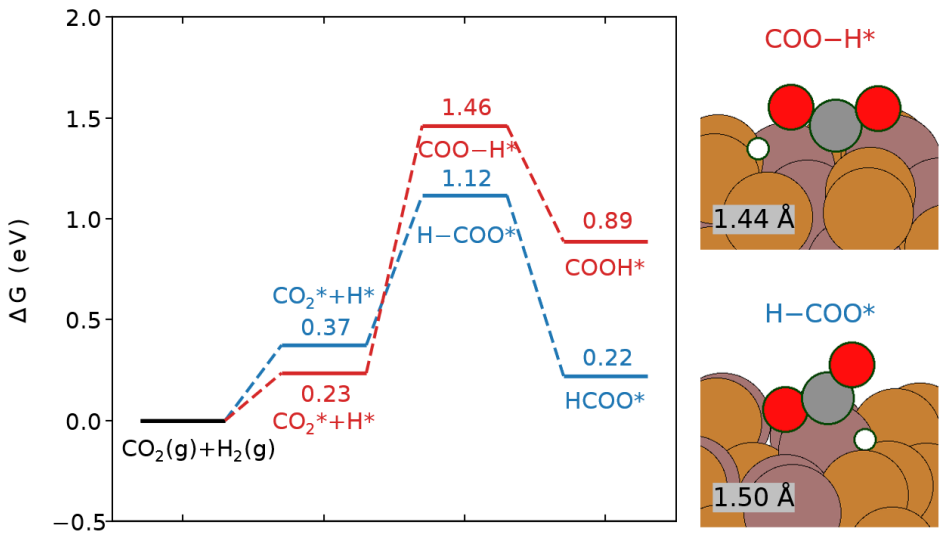

Fig. S23. Gibbs free energy diagram and transition state structures for the initial steps of CO_2 hydrogenation on Cu_7In_3(040)-b at 500 K under partial pressures of 22.5 bar H_2 and 7.5 bar CO_2. The color scheme of atoms is as follows: Cu, orange; In, brown; O, red; C, gray; H, white.

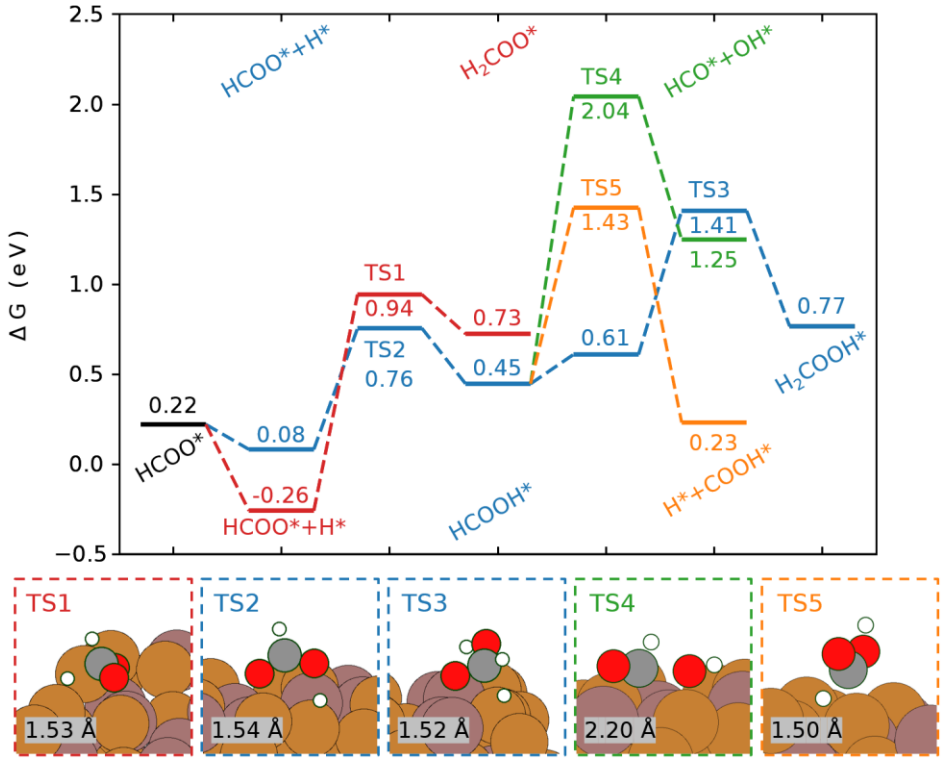

Fig. S24. Gibbs free energy diagram and representative transition state structures for competing reaction pathways originating from HCOO* on Cu_7In_3(040)-b at 500 K, including hydrogenation and dissociation routes relevant to CO_2 hydrogenation. The color scheme of atoms: Cu, orange; In, brown; O, red; C, gray; H, white.

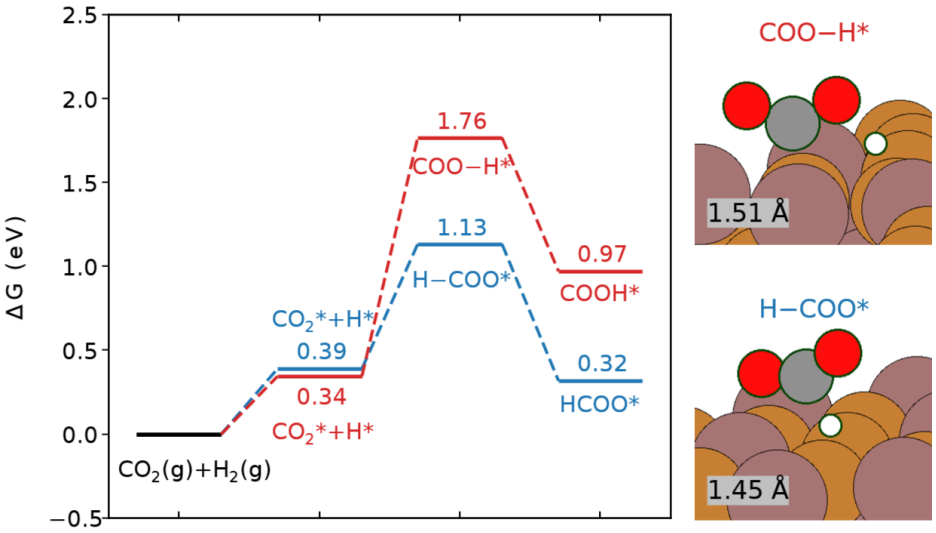

Fig. S25. Gibbs free energy diagram and transition state structures for the initial steps of CO_2 hydrogenation on $Cu_{11}In_9$(020) at 500 K under partial pressures of 22.5 bar H_2 and 7.5 bar CO_2. The color scheme of atoms is as follows: Cu, orange; In, brown; O, red; C, gray; H, white.

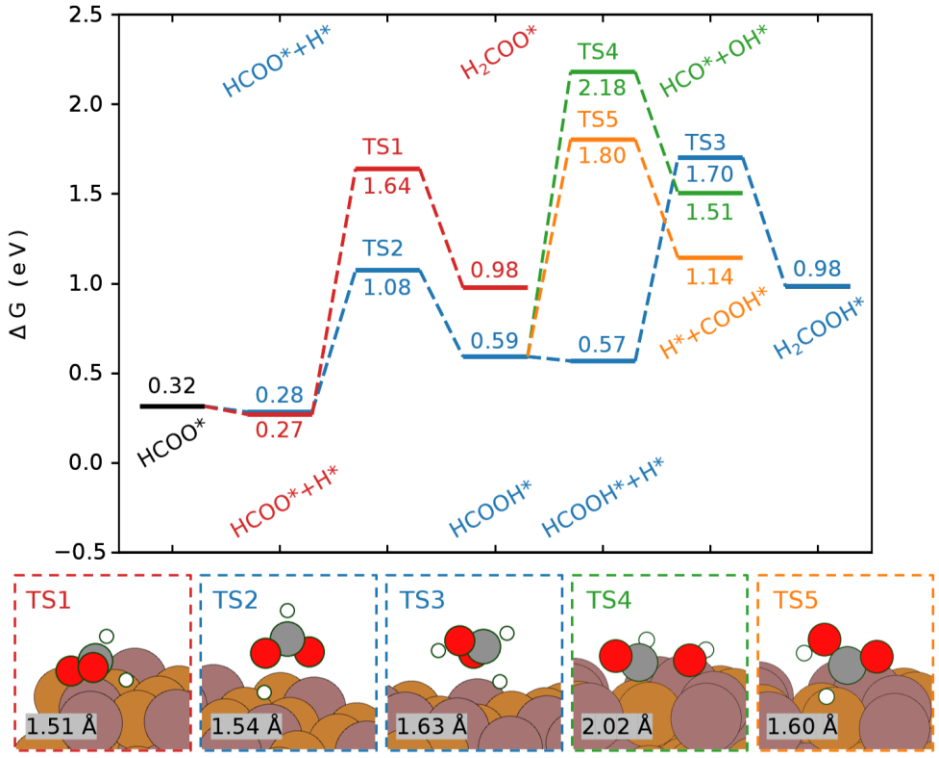

Fig. S26. Gibbs free energy diagram and representative transition state structures for competing reaction pathways originating from HCOO* on $Cu_{11}In_9$(020) at 500 K, including hydrogenation and dissociation routes relevant to CO_2 hydrogenation. The color scheme of atoms: Cu, orange; In, brown; O, red; C, gray; H, white.

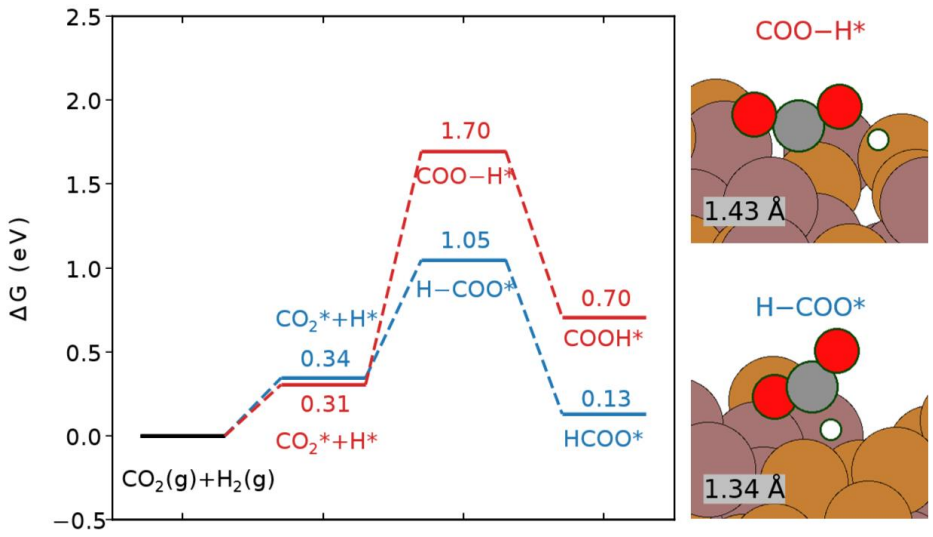

Fig. S27. Gibbs free energy diagram and transition state structures for the initial steps of CO_2 hydrogenation on $Cu_{11}In_9(551)$ at 500 K under partial pressures of 22.5 bar H_2 and 7.5 bar CO_2. The color scheme of atoms is as follows: Cu, orange; In, brown; O, red; C, gray; H, white.

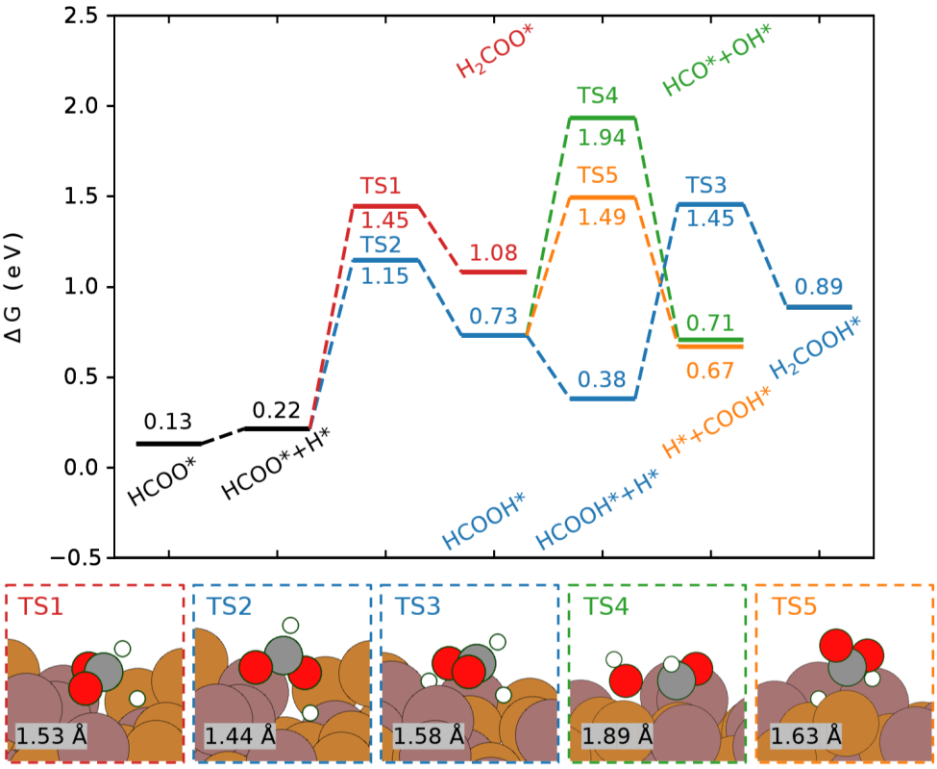

Fig. S28. Gibbs free energy diagram and representative transition state structures for competing reaction pathways originating from HCOO* on $Cu_{11}In_9(551)$ at 500 K, including hydrogenation and dissociation routes relevant to CO_2 hydrogenation. The color scheme of atoms: Cu, orange; In, brown; O, red; C, gray; H, white.

6. Extended analysis and validation of the G_{HL} descriptor

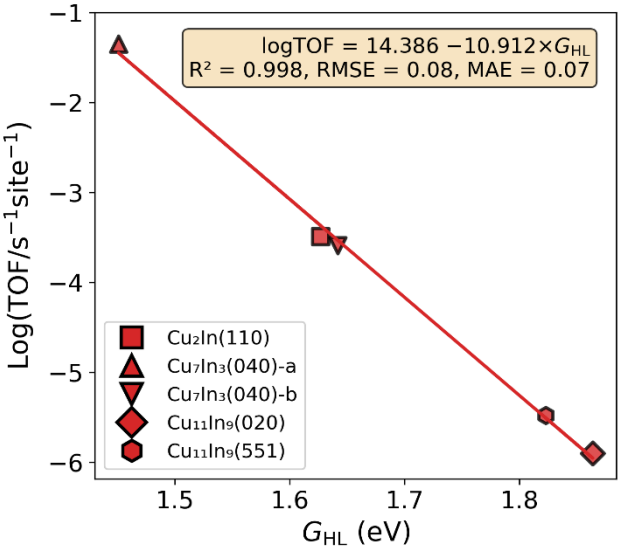

Fig. S29. Correlation between the logarithm of the reaction rates and the G_{HL} descriptor for methanol formation across five Cu−In surfaces at 500 K.

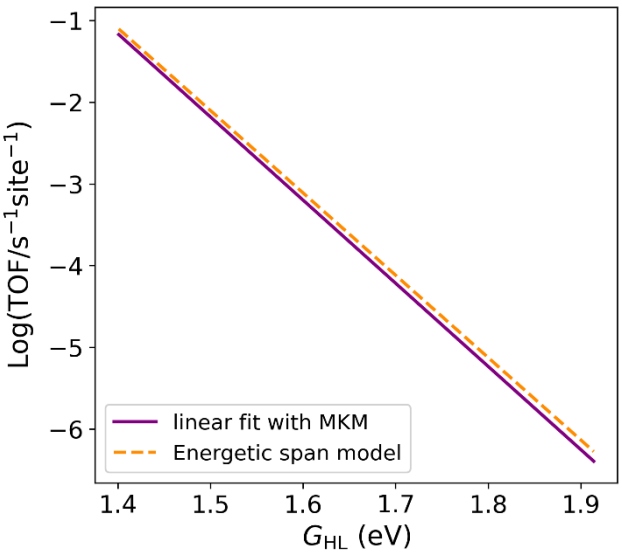

Fig. S30. Comparison between the linear fit obtained from the G_{HL} descriptor and MKM-derived TOFs and the rate–barrier relationship predicted directly from the energetic span model at 500 K.

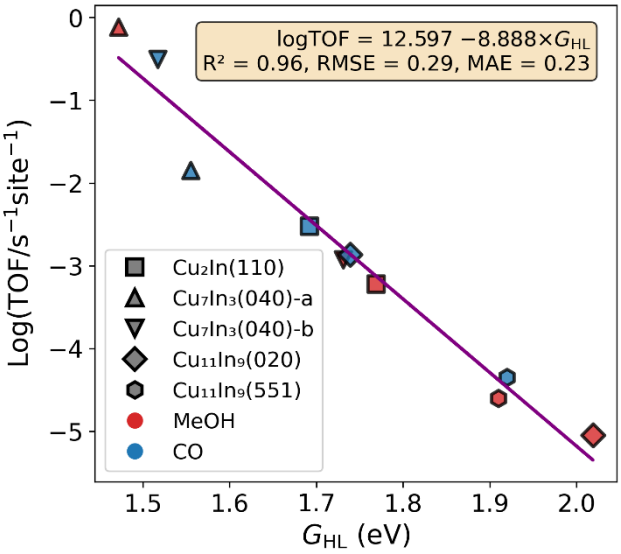

Fig. S31. Correlation between the logarithm of the reaction rates and the G_{HL} descriptor for methanol and CO formation across five Cu−In surfaces at 550 K.

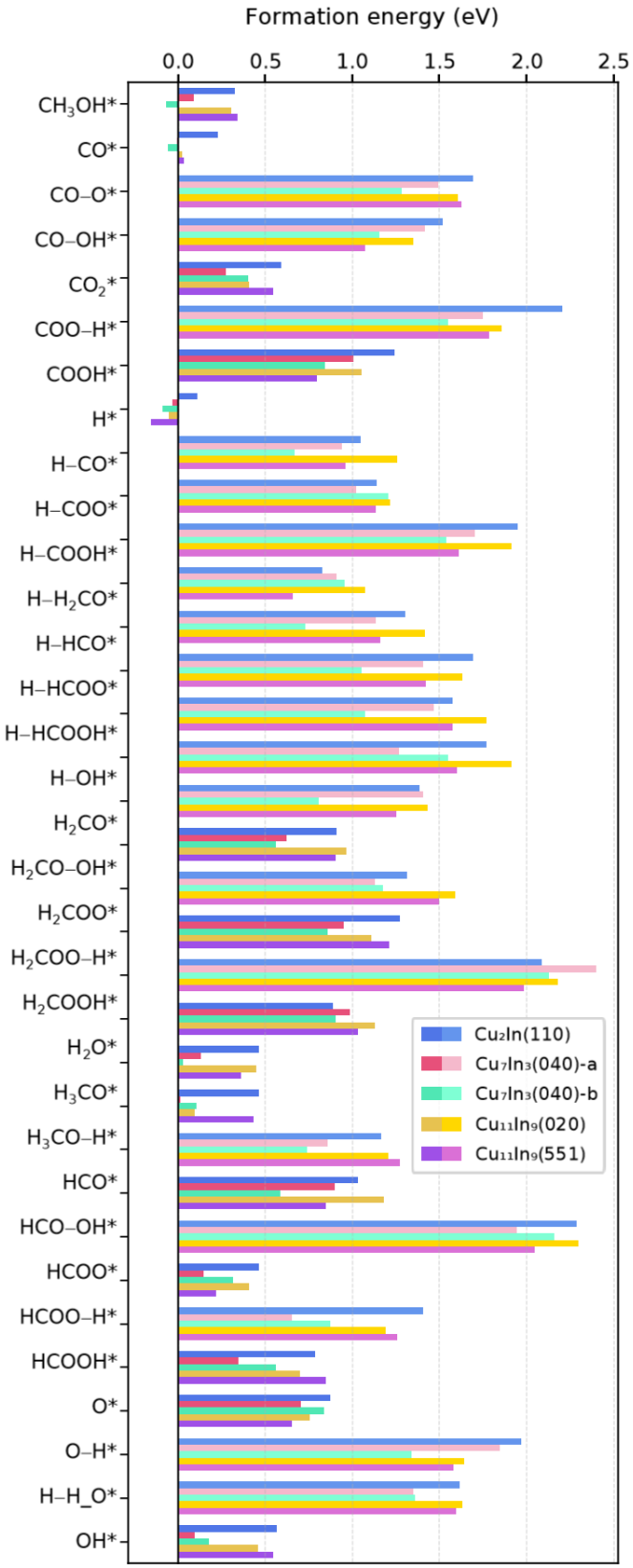

Fig. S32. Relative Gibbs free energies of formation of surface intermediates and transition states at 550 K, evaluated with respect to the gas-phase chemical potentials (H_2, CO_2, H_2O) under reaction conditions with partial pressures of 22.5 bar H_2, 7.5 bar CO_2, and 1 bar each of CO, H_2O, and MeOH. Dark-colored bars denote intermediates, while light-colored bars represent transition states.

Note:

At 550 K, H* is identified as the lowest-formation-energy intermediate on all surfaces, resolving the H_3CO* deviation observed on Cu_7In_3(040)-a at 500 K.